REVISED VERSION 1

1 **HOW GEOMETRY AND ANISOTROPY AFFECT RESIDUAL STRAIN IN HOST-**

2 **INCLUSION SYSTEM: COUPLING EXPERIMENTAL AND NUMERICAL**

3 **APPROACHES**

4 N. Campomenosi[1], M.L. Mazzucchelli[2], B.D. Mihailova[3], M. Scambelluri [1], R.J. Ange1[2], F.

5 Nestola[4], A. Reali[5], M. Alvaro[2]

6 [1]*Department of Earth Science, Environment & Life, University of Genoa, Corso Europa 26, 16132*
7 *Genoa, Italy.*
8 [2]*Department of Earth and Environmental Sciences, University of Pavia, Via A. Ferrata, 1 I-27100*
9 *Pavia, Italy,*
10 [3]*Department of Earth Sciences, University of Hamburg, Grindelallee 48, D-20146 Hamburg,*
11 *Germany.*
12 [4]*Department of Geosciences, University of Padova, Via G. Gradenigo 6, I-35131 Padova, Italy.*
13 [5]*Department of Civil Engineering and Architecture, University of Pavia, Via A. Ferrata 3, I-27100*
14 *Pavia, Italy*
15
16

17 *Corresponding author:* matteo.alvaro@unipv.it

18 **Abstract**

19 Raman spectroscopy provides information on the residual strain state of host-inclusion systems that,

20 coupled with the elastic geobarometry theory, can be used to retrieve the *P-T* conditions of inclusion

21 entrapment. In-situ Raman measurements of zircon and coesite inclusions in garnet from the

22 Ultrahigh-pressure Dora Maira Massif show that rounded inclusions exhibit constant Raman shifts

23 throughout their entire volume. In contrast, we demonstrate that Raman shifts can vary from the

24 center to the edges and corners of faceted inclusions. Step-by-step polishing of the garnet host show

25 that the strain in both rounded and prismatic inclusions is gradually released as the inclusion

26 approaches the free surface of the host. More importantly our experimental results coupled with

27 selected numerical simulations demonstrate that the magnitude and the rate of the strain release

28 depends also on the contrast in elastic properties between the host and the inclusion and on the

29 inclusion crystallographic orientation with respect to the external surface. These results allowed us to

30 give new methodological guidelines for determining the residual strain in host inclusion systems.

31

32 **Keywords:** elastic barometry; inclusion; Raman spectroscopy; zircon; garnet; coesite; Dora Maira

33 Massif; Ultra High Pressure metamorphism;

34 **Introduction**

35 Elastic geobarometry for host-inclusion systems is based on measurements of the

36 residual strains produced during exhumation as a consequence of the contrast in elastic

REVISED VERSION 1

37   properties between the host and the inclusion. The residual strain in the inclusions can be

38   measured by micro-Raman spectroscopy or X-ray diffraction and can be used to provide

39   estimates of pressure and temperature (*P-T*) conditions for metamorphic rocks that are not

40   dependent on chemical equilibrium (e.g., Rosenfeld and Chase, 1961; Enami et al., 2007;

41   Angel et al., 2015; Anzolini et al., 2018; Murri et al., 2018). Models for elastic geobarometry

42   only apply to the simple case of elastically isotropic host-inclusion pairs with a simple ideal

43   geometry where a small spherical inclusion is trapped in an infinite host (Angel et al., 2015).

44   Recent numerical models showed that any deviations from the idealized geometry

45   significantly affects the estimation of "residual pressure" (Mazzucchelli et al., 2018). Indeed,

46   gradients in non-spherical inclusions have been already reported (e.g. Zhukov and Korsakov,

47   2015; Murri et al., 2018). Moreover, several studies pointed out the effects on the residual

48   "pressure" determination of the inclusion size and its partial exposure with respect to the

49   mineral host surface (e.g. Rosenfeld and Chase, 1961; Enami et al., 2007; Zhang, 1998;

50   Mazzucchelli et al. 2018). Nevertheless, open questions still remain, including: what is the

51   effect of the inclusion anisotropy on the residual strain release? How much can the contrast

52   in properties between the host and the inclusion and their geometry influence the residual

53   strain? Therefore, we propose an alternative way to test the effect of the geometry of the

54   host-inclusion system on the Raman signal and on the calculated residual pressure upon

55   polishing: to collect spectra from selected inclusions with different shape, size and

56   crystallographic orientation, while performing several steps of polishing of the rock thick

57   section to bring the inclusion closer to the external surface of the host.

58   In this manuscript we report the Raman spectra of rounded and elongated zircon

59   inclusions and a rounded coesite inclusion in pyrope from the ultrahigh-pressure (UHP)

60   Alpine Dora Maira Massif measured before and after several subsequent steps of polishing.

61   The measured "residual pressures" are compared with the results of a set of Finite Element

62   models following the approach of Mazzucchelli et al. (2018). This allows us to provide new

63   methodological guidelines and examples of correction curves to adjust measurements carried

64   out on faceted and anisotropic inclusions and/or close to the host surface.

65

66   **Sample description**

67   We analyzed zircon and coesite inclusions within pyrope megablasts and

68   porphyroblasts respectively, from the whiteschist of the Brossasco-Isasca UHP unit in the

69   Gilba locality, whose petrography and petrology were reported by several authors (e.g.

70   Chopin, 1984; Hermann, 2003). Whiteschists occur as lenses inside ortho-gneiss and para-

71   gneiss of the Monometamorphic Complex (data repository) and mainly consist of quartz,

72   phengite, kyanite and porphyroblastic to megablastic pyrope-rich garnet. The Dora Maira

73   whiteschist shows a phengite, garnet and kyanite-bearing foliation that wraps around the

74   garnet megablasts (up to 15 cm across). The latter contain numerous inclusions (from few

75   microns to 1 mm in size) mainly of kyanite, rutile and zircon. Garnet porphyroblasts (up to 2

76   mm in size) within the foliated rock matrix contain rutile, zircon and coesite inclusions.

77   Coesite grains are frequently surrounded by quartz rims and palisade quartz structures

78   (Chopin, 1984), but we only measured the rare monocrystalline unaltered coesite inclusions.

79   For the application of elastic geobarometry we selected garnet-core and rim domains

80   unaltered and free of fractures. In these domains, the coesite and zircon inclusions are

81   surrounded by birefringent haloes (Figure 1), indicating that the structure of the garnet host

82   around the inclusions is anisotropically strained.

83

84   **Methods**

85   As pointed out previously (Zhang, 1998; Mazzucchelli et al., 2018), only small

86   isolated inclusions far from any free surface of the garnet thick sections (e.g. distance > 3

REVISED VERSION 1

87   radii of the inclusion) do not suffer potential strain release. Therefore, for this study we

88   prepared polished sections of 250-260 μm thickness. We performed Raman spectroscopic

89   measurements only on inclusions at the center of the section with a mean linear size smaller

90   than 50 μm, (i.e. considerably less than the distance to the host surface).

91   Micro-Raman scattering measurements were conducted in backscattering geometry

92   with a Horiba Jobin-Yvon T64000 triple-monochromator spectrometer with a spectral

93   resolution of ~2 cm^{-1} and instrumental accuracy in peak positions of ~0.35 cm^{-1}. For each

94   inclusion, a series of spot measurements were carried out along the equatorial plane of the

95   inclusion as shown in Figure 2. Details of the measurements and data processing are given in

96   the supplementary materials.

97   We collected Raman spectra before and after polishing of the garnet hosts by known

98   amounts. The inclusion distance from the surface (i.e. the distance between the equatorial

99   plane of the inclusion and the host external surface) was estimated by means of optical focus

100   coupled with the controlled z-position motorized microscope stage. We repeated the

101   procedure until the inclusion was half-exposed. This allowed us to observe the "real time"

102   evolution of the strains inside the inclusions in terms of changes in the Raman frequencies.

103   Here we show examples of single crystals of zircon: one rounded (20   μm radius) and one

104   prismatic (80   μm along the long axis), labelled S2 and S3, respectively and one rounded

105   single crystal of coesite (15   μm radius, sample S24) in the garnet megablasts and

106   porphyroblasts, respectively. No prismatic or idiomorphic coesite inclusions have been

107   found. Since our inclusions are elastically anisotropic, their orientation with respect to the

108   polishing surface is critical for the interpretation of the results by means of numerical

109   simulations. The idiomorphic zircon grain S3 has the *c* axis inclined with respect to the

110   polishing surface by approximately 20° (estimated optically). Analysis of the peak intensities

111   in the polarized Raman spectra suggests that the rounded zircon grain S2 has its *c* axis

REVISED VERSION 1

112   almost perpendicular to the surface. The coesite crystal S24 was rounded and the absence of

113   pronounced changes in the Raman intensities measured in different scattering geometries

114   makes it impossible to determine its orientation and therefore it was not possible to perform

115   numerical simulations for this inclusion.

116   Finite element simulations have been carried out to support the interpretation of our

117   measurements of zircon inclusions S2 and S3 and to evaluate the effect of the proximity of

118   the inclusion to the external surface of the thick section on the residual strain of the inclusion

119   (procedures as in Mazzucchelli et al., 2018, further details are reported in data repository).

120   Elastic anisotropy has been incorporated in the model for the zircon inclusions. The pyrope

121   host was treated as isotropic because its universal elastic anisotropy index (Ranganathan and

122   Ostoja-Starzewski, 2008) is negligible (i.e. 9×10^{-4}), based on the elastic moduli reported by

123   Sinogeikin and Bass (2002). The use of isotropic elastic properties for the host allows us to

124   neglect the mutual crystallographic orientation of the host and the inclusion. For our

125   purposes, the only relevant orientation is that of the inclusion with respect to the surface of

126   the petrographic section.

127

128   **Results and discussion**

129   Both rounded and idiomorphic inclusions close to the center of the section display Raman

130   peak positions shifted toward higher wavelengths compared to free reference crystals. Within

131   the instrumental precision (± 0.35 cm^{-1}), the rounded zircon inclusion S2 and the rounded

132   coesite inclusion S24 showed no spatial variation of the Raman peak positions within the

133   inclusions. On the other hand, for idiomorphic crystals (zircon inclusion S3 with well-

134   developed corners and edges) there is a steady increase in the peak positions of about 1 cm^{-1}

135   from the center towards the edges of the inclusions (Figure 2 B). This is a direct

136   consequence of strain heterogeneity in the inclusion, which can be caused by chemical

137   zonation, zoned radiation-induced damage and/or an imposed strain gradient.   The

138   substitution of elements such as Th, U, or Hf for Zr, may cause expansion (U, Th) or

139   contraction (Hf) of the zircon unit cell (Nasdala et al., 1998), leading to a change in the

140   phonon wavenumbers. However, compositional analysis of the exposed grain performed

141   after the final step of polishing did not reveal any chemical zonation (see supplementary

142   material). Radioactive decay of elements such as U and Th can induce structural damage,

143   leading to Raman peak broadening and a shift towards lower wavenumbers (Binvignat et al.,

144   2018). However, the full-width-at-half-maximum (FWHM) of a given phonon mode for

145   totally entrapped S3 remains the same throughout the entire grain and within the

146   instrumental spectral resolution and is equal to that of well crystalline zircon (Binvignat et

147   al., 2018), thus indicating a high degree of crystallinity throughout the entire grain bulk.

148   Since the zircon inclusion S3 is chemically homogeneous (see Appendix A.1) and well-

149   crystalline, the variable Raman shift in it is due to its faceted shape (Eshelby, 1957), because

150   the edges and corners act as stress concentrators (Zhang, 1998; Mazzucchelli et al., 2018).

151   After polishing the Raman spectra of S3 became homogeneous within the fully exposed part

152   of the sample (Figure 2 B), confirming that the variation in the peak position in a single

153   crystal for all bands was caused by the shape of the crystal.

154   A decrease in the Raman band wavenumbers was measured at the center of the inclusions

155   upon polishing for all the investigated samples of zircon and coesite. As an example, Figure

156   3A shows the B_{1g} mode near 1008 cm^{-1} measured on zircon sample S3 at three different steps

157   of polishing. Strictly speaking, the phonon wavenumbers are directly related to the strain,

158   rather than to the applied pressure. Moreover, for elastically anisotropic materials the same

159   relative volume change can be obtained by different strains, for example as induced by

160   hydrostatic or deviatoric stress. Therefore, the commonly used direct proportionality

161   between the Raman peak positions and residual pressure is a strongly oversimplified

162 assumption (Murri et al., 2018). Nonetheless, if we assume that the change in Raman

163 wavenumber ω is linear with mean stress P (i.e. $\frac{\partial \omega}{\partial P}$ is constant), we can introduce the

164 normalized change in the peak position $\Delta\omega_{norm}$ as a parameter to express the relative

165 release in "pressure" as the inclusion becomes closer to the external surface of the host

166 during polishing:

167

$$\Delta\omega_{norm} = \frac{\left((\omega_{I,d} - \omega_{I,0})\frac{\partial P}{\partial \omega} - (\omega_{I,\infty} - \omega_{I,0})\frac{\partial P}{\partial \omega}\right)}{(\omega_{I,\infty} - \omega_{I,0})\frac{\partial P}{\partial \omega}} = \frac{P_{I,d} - P_{I,\infty}}{P_{I,\infty}}$$

$$= \frac{(\omega_{I,d} - \omega_{I,\infty})}{(\omega_{I,\infty} - \omega_{I,0})} = \Gamma$$

(1)

168

169 Where   is the wavenumber for a free crystal measured at ambient conditions,   and

170   are the wavenumber and the corresponding pressure for an inclusion in an infinitely

171 large host (i.e. before the polishing, when the inclusion was far from the surface of the host),

172 while   and   are the wavenumber measured on the inclusion and its pressure after

173 each polishing step and associated to a specific normalized distance d (i.e. the distance from

174 the inclusion center to the host external surface divided by the corresponding inclusion

175 radius). Under these assumptions, equation (1) shows that $\Delta\omega_{norm}$ becomes equivalent to

176 the geometrical factor Γ defined by Mazzucchelli et al. (2018).

177 As can be seen in Figure 3 B and C, the normalized change in the peak position $\Delta\omega_{norm}$

178 decreases progressively towards -1 (i.e. the Raman shift becomes equal to that of the free

179 inclusion), when the inclusion approaches the host surface. The trends of "pressure" release

180 estimated from the Raman spectra measured on our zircon samples show the same pattern

181 with those calculated from numerical simulations performed on similar geometries and

182   crystallographic orientations (e.g. see the dotted lines in fig. 3 B). However, the experimental

183   data suggest a greater amount of stress release compared to the numerical simulations. For

184   example, at a normalized distance of 1 (inclusion just in contact with the external surface),

185   the calculated stress release is approximately 50%, whereas that obtained from experimental

186   data is about 70% (fig. 3 A). There are at least two contributions to this discrepancy: (i) for

187   non-cubic inclusions, direct conversion of Raman shifts into pressures using a hydrostatic

188   calibration is incorrect; (ii) when the inclusion is close to the surface, strain gradients may be

189   relaxed through plasticity or micro-fractures that are not considered in our purely elastic

190   numerical models. Interestingly, our experiments show that even after partial exposure of the

191   inclusion (i.e. for normalized distances $\leq$ 1) the Raman shift does not record full strain

192   release (i.e. the inclusion is not at ambient conditions). In Figure 3 C, for example, the

193   polished coesite inclusion still shows 40% of its original residual strain. Finally, the

194   difference in the strain release between zircon and coesite inclusions is probably due to the

195   different contrast in properties with respect the host garnet. Indeed, since coesite is softer

196   than zircon, the host garnet can still retain a greater amount of its residual strain even if half

197   of the inclusion is exposed. This implies the possibility to have thinner hosts for softer

198   inclusions such as coesite or quartz in garnet but, however, the possibility of fracturing

199   during polishing is high (Enami et al., 2007).

200

201   **Implications**

202   Our measurements show that Raman shift is homogeneous only in rounded inclusions while

203   it is non-homogeneous in faceted ones (Figure 2 A and B), in a full agreement with

204   numerical calculations (Mazzucchelli et al. 2018) and theory (Eshelby, 1957). Therefore,

205   multiple Raman spectra collected on faceted inclusions should not be averaged if their

206   differences are larger than the instrumental peak precision. Instead, to avoid the effects of

207   grain shape on Raman peak positions, only Raman spectra measured at the center of the

208   inclusions should be used because there we can apply the geometrical correction (see

209   Mazzucchelli et al., 2018).

210   Our polishing experiments confirm that the Raman shift on the inclusion decreases as the

211   inclusion gets closer to the external surface (Rosenfeld and Chase, 1961; Zhang, 1998;

212   Mazzucchelli et al., 2018). Therefore, only inclusions whose centers are distant more than 4

213   radii (Figure 3 B) from the section surface and internal surfaces of the host should be used. If

214   the Raman peak positions vary from one inclusion to another, even when the inclusions are

215   properly selected, this indicates that some other factor is responsible, such as chemical

216   variation in the host or inclusions, or growth of the host and thus inclusion entrapment under

217   different conditions, such as along a prograde subduction path. More importantly, our

218   results, coupled with our FE numerical simulations, show how anisotropy (i.e.

219   crystallographic orientation of the inclusion with respect to the external surface) and the

220   contrast between the inclusion and host physical properties influences the strain release

221   during polishing. Furthermore, even when an inclusion is exposed at the surface of the host

222   grain, it can still exhibit a variation in the peak position with respect to a free crystal, and

223   thus residual strains and stresses (Figure 3 C). Therefore, partially entrapped grains as a

224   strain free standard should be avoided or chosen very carefully against which to measure the

225   Raman shifts of unexposed inclusions.

226   Finally, as an example, if we calculate from our experimental Raman shift values the strain

227   and then the mean stress in the inclusion after subsequent polishing steps, following the

228   approach given by Murri et al. (2018), the zircon S3 has an initial residual pressure (P_{inc})

229   before polishing of 0.5 GPa. After 55 microns of polishing (1.5 of normalized distance in

230   figure 3 B), when the inclusion is still buried in its garnet host, the P_{inc} drops to 0.2 GPa. A

231   value of 0.06 GPa is recorded when the inclusion is half exposed. For zircon S2 the initial

REVISED VERSION 1

232   P_{inc} was about 0.9 GPa and about 0.3 GPa when the inclusion was just touching the external

233   surface of the host. In the supplementary material a table showing the evolution of the P_{inc} as

234   function of the polishing for the two zircon inclusions is reported (Table S.8). For coesite no

235   reliable data are available to give the strain state of the inclusion from the Raman peak

236   positions.

237

238   <div align="center">**Acknowledgments**</div>

239

251

252   <div align="center">**References**</div>

253 Angel, R.J., Nimis, P., Mazzucchelli, M.L., Alvaro, M., and Nestola, F., 2015, How large are

254   departures from lithostatic pressure? Constraints from host-inclusion elasticity.

255   Journal of Metamorphic Geology, 33, 801–813.

256 Anzolini, C., Prencipe, M., Alvaro, M., Romano, C., Vona, A., Lorenzon, S., Smith, E. M.,

257   Brenker, F. E., Nestola, F., 2018, Depth of formation of super-deep diamonds:

258   Raman barometry of $CaSiO_3$-walstromite inclusions. American Mineralogist, 103(1):

259   69-74.

260 Chopin, C., 1984, Coesite and pure pyrope in high-grade blueschists of the Western Alps: a

261   first record and some consequences. Contributions to Mineralogy and Petrology, 86,

262   107–118.

263 Binvignat F. A. P., Malcherek T., Angel R. J., Paulmann C., Schlüter J. Mihailova B. D.,

264 2018

265   Radiation damaged zircon under high pressures. Physics and Chemistry of

266   Minerals.

267 Enami, M., Nishiyama, T., and Mouri, T., 2007, Laser Raman microspectrometry of

268   metamorphic quartz: A simple method for comparison of metamorphic pressures.

269   American Mineralogist, 92, 1303–1315.

270 Eshelby, J. D., 1957, The determination of the elastic field of an ellipsoidal inclusion and

271   related problems. Proceedings of the Physical Society of London, Series A, 241, 376-

272   396.

273 Hermann, J., 2003, Experimental evidence for diamond-facies metamorphism in the Dora-

274   Maira massif. Lithos, 70, 163-182.

275 Mazzucchelli, M.L., Burnley, P., Angel, R.J., Morganti, S., Domeneghetti, M.C., Nestola, F.,

276   and Alvaro, M., 2018, Elastic geothermobarometry: Corrections for the geometry of

277   the host-inclusion system. Geology, 46(3), 231-234.

278 Murri M., Mazzucchelli M. L., Campomenosi, N., Korsakov, A. V., Prencipe, M.,

279   Mihailova, B. D., Scambelluri, M., Angel, R. J., and Alvaro, M., 2018 Raman elastic

280   geobarometry for anisotropic mineral inclusions. American Mineralogist, in press

281 Nasdala, L., Pidgeon, R.T., Wolf, D., and Irmer, G., 1998, Metamictization and U-Pb

282   isotopic discordance in single zircons: a combined Raman microprobe and SHRIMP

283   ion probe study. Mineralogy and Petrology, 62, 1–27.

284 Rosenfeld, J.L. & Chase, A.B., 1961. Pressure and temperature of crystallization from elastic

285   effects around solid inclusion minerals? American Journal of Science, 259, 519-541.

286 Sinogeikin, S. V., and Bass, J.D., 2002, Elasticity of pyrope and majorite-pyrope solid

287   solutions to high temperatures. Earth and Planetary Science Letters, 203, 549-555.

288 Zhang, Y., 1998. Mechanical and phase equilibria in inclusion–host systems. Earth and

289   Planetary Science Letters, 157, 209-222.

290 Zhukov, V. P., & Korsakov, A. V. (2015). Evolution of host inclusion systems: a visco

291   elastic model. Journal of Metamorphic Geology, 33(8), 815-828.

292

293 **Figure captions**

294 **Figure 1.** A polished pyrope megablast section with partial talc + chlorite alteration along

295 fractures and rims. The red square shows an example of a mm-sized fracture-free garnet area

296 selected for this study, in which zircon and coesite crystalline inclusions exhibiting strain-

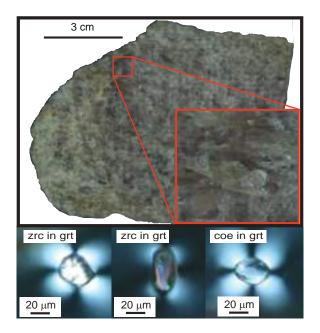297 induced birefringent haloes in the surrounding host have been found.

298

299 **Figure 2.** Position of the Raman peak $A_{1g} \sim 975$ cm^{-1} in a rounded (A) and an idiomorphic

300 (B) zircon crystal before and after the final step of polishing. The solid lines in the plots are

301 guides for the eye; the dashed line in (B) traces the data points measured after two days of

302 final exposure of the grain.

303

304 **Figure 3.** (**A**) Raman scattering arising from the antisymmetric SiO$_4$ stretching (the B$_{1g}$

305 crystal phonon mode ~ 1008 cm^{-1}) measured when the grain S3 was fully entrapped (red

REVISED VERSION 1

306   line), at an intermediate stage of polishing (yellow), and when the inclusion was exposed at

307   the final stage of polishing (green line). The numbers are the measured Raman shifts. **(B)**

308   Measured normalized wavenumber shifts $\Delta\omega_{norm}$ for zircon S2 (green circles) and zircon S3

309   (blue squares) versus the normalized distance d to the host surface along with gaussian fits to

310   the corresponding data $A_{1g} \sim 975$ and $B_{1g} \sim 1008$ cm^{-1} data sets (solid lines) as well as the

311   calculated geometrical factor Γ (dashed lines) from the FE model; $\Delta\omega_{norm}(d)$ and $\Gamma(d)$ show

312   the same trend within uncertainties. (C) Measured $\Delta\omega_{norm}(d)$ (red circles) and a gaussian fit

313   to $A_{1g} \sim 119$ and ~ 521 cm^{-1} (solid line) for S24 coesite inclusion

314

315